

# Geophysical Research Letters

## RESEARCH LETTER

10.1029/2020GL090936

### Key Points:

- First in situ observation of a nascent tropical tropopause cirrus
- Homogeneous formation of tiny ice crystals ( $<1 \mu\text{m}$ ) is due to a short vertical scale gravity wave at the tropopause
- Such optically thin cirrus clouds would be missed by current aircraft instruments/remote sensing systems

### Supporting Information:

- Supporting Information S1

### Correspondence to:

I. Reinares Martínez,  
[irene.reinares@univ-reunion.fr](mailto:irene.reinares@univ-reunion.fr)

### Citation:

Reinares Martínez, I., Evan, S., Wienhold, F. G., Brioude, J., Jensen, E. J., Thornberry, T. D., et al. (2021). Unprecedented observations of a nascent in situ cirrus in the tropical tropopause layer. *Geophysical Research Letters*, 48, e2020GL090936. <https://doi.org/10.1029/2020GL090936>

Received 22 SEP 2020

Accepted 5 DEC 2020

## Unprecedented Observations of a Nascent In Situ Cirrus in the Tropical Tropopause Layer

I. Reinares Martínez<sup>1</sup> , S. Evan<sup>1</sup> , F. G. Wienhold<sup>2</sup> , J. Brioude<sup>1</sup> , E. J. Jensen<sup>3</sup> , T. D. Thornberry<sup>4,5</sup> , D. Héron<sup>1</sup>, B. Verreyken<sup>1,6,7</sup>, S. Körner<sup>8</sup>, H. Vömel<sup>3</sup> , J.-M. Metzger<sup>9</sup>, and F. Posny<sup>1</sup> 

<sup>1</sup>LACy, Laboratoire de l'Atmosphère et des Cyclones, UMR8105, CNRS, Université de La Réunion, Saint-Denis, France, <sup>2</sup>Institute for Atmospheric and Climate Science, ETH, Zurich, Switzerland, <sup>3</sup>National Center for Atmospheric Research, Boulder, CO, USA, <sup>4</sup>Chemical Sciences Laboratory, NOAA Earth System Research Laboratory, Boulder, CO, USA, <sup>5</sup>Cooperative Institute for Research in Environmental Sciences, University of Colorado Boulder, Boulder, CO, USA, <sup>6</sup>Royal Belgian Institute for Space Aeronomy, Brussels, Belgium, <sup>7</sup>Department of Chemistry, Ghent University, Ghent, Belgium, <sup>8</sup>Deutscher Wetterdienst, Meteorological Observatory Lindenberg, Lindenberg, Germany, <sup>9</sup>Observatoire des Sciences de l'Univers de La Réunion, UMS3365, CNRS, Université de La Réunion, Saint-Denis, France

**Abstract** A nascent in situ cirrus was observed on January 11, 2019 in the tropical tropopause layer (TTL) over the southwestern Indian Ocean, with the use of balloon-borne instruments. Data from cryogenic frost point hygrometer (CFH) and Compact Optical Backscatter and Aerosol Detector (COBALD) instruments were used to characterize the cirrus and its environment. Optical modeling was employed to estimate the cirrus microphysical properties from the COBALD backscatter measurements. Newly formed ice crystals with radius  $<1 \mu\text{m}$  and concentration  $\sim 500 \text{ L}^{-1}$  were reported at the tropopause. The relatively low concentration and CFH ice supersaturation (1.5) suggests a homogeneous freezing event stalled by a high-frequency gravity wave. The observed vertical wind speed and temperature anomalies that triggered the cirrus formation were due to a 1.5-km vertical-scale wave, as shown by a spectral analysis. This cirrus observation shortly after nucleation is beyond remote sensing capabilities and presents a type of cirrus never reported before.

**Plain Language Summary** Ice clouds are very common in the tropical tropopause layer, a layer of the atmosphere between 14 and 18 km separating the troposphere and the stratosphere. Ice clouds can be formed in situ, generated by cold temperature anomalies due to atmospheric disturbances. In this observational study, we use data from instruments that were flown on the same balloon on January 11, 2019 from Réunion Island, in the southwestern Indian Ocean. We report an ice cloud at the tropopause, at  $\sim 16.5 \text{ km}$ , composed of ice particles with a concentration of more than 500 per liter. This suggests that the ice cloud formed by homogeneous freezing, that is, the freezing of airborne aqueous solutions. In addition, an abrupt increase in ascent rate of the balloon is related to an atmospheric disturbance which cooled the air and possibly led to the ice cloud formation. The tiny size of the ice crystals indicates that they have just formed. This is a very rare observation because nucleation events are very short.

## 1. Introduction

In situ cirrus formation in the tropical tropopause layer (TTL, Fueglistaler et al., 2009) occurs as rising air masses reach this extremely cold region (Brewer, 1949; Jensen & Pfister, 2004; Jensen et al., 1996). Cirrus formation and sedimentation contribute to water vapor transport in the TTL, and its entrance value into the low stratosphere, where it has a nonnegligible greenhouse effect (Dessler et al., 2013; Forster & Shine, 2002; Solomon et al., 2010). However, the interaction between different-scale dynamical processes driving temperature anomalies in the TTL and the unknown composition of the TTL render the understanding of the cirrus formation very challenging.

Cirrus formation can occur either by homogeneous or heterogeneous ice nucleation mechanisms. For homogeneous freezing of aqueous aerosols, occurring at temperatures below  $-38^\circ\text{C}$ , theoretical models (e.g., Kärcher & Lohmann, 2002) predict that ice concentrations depend on the cooling rate, rather than on the concentration of aqueous solution droplets, which is rarely a limiting factor. Homogeneous nucleation generally requires conditions of supersaturation above 160% for TTL temperatures (Koop et al., 2000). On

the other hand, heterogeneous nucleation depends strongly on the population of ice forming nuclei (IFN, Cziczo et al., 2013; Jensen et al., 2016b), which can be active at much lower supersaturations, but whose abundance is typically limited.

Observations of cirrus in the TTL show that ice concentrations are generally below  $100 \text{ L}^{-1}$  (e.g., Krämer et al., 2009; Woods et al., 2018). In their recent climatology, Krämer et al. (2020) find median values of ice concentration between 10 and  $100 \text{ L}^{-1}$ . These values are well below expected numbers for purely homogeneous nucleation. To explain these results, it has been suggested that the main mechanism for low-concentration cirrus formation is heterogeneous nucleation (Cziczo et al., 2013), which is constrained by IFN concentrations. Experimental results reported by DeMott et al. (2003) show median values of heterogeneous IFN concentrations of  $\sim 10 \text{ L}^{-1}$  in the free troposphere. Similar measurements have not been made in the TTL, although lower concentrations are expected (Froyd et al., 2009). Several studies have shown, using a box model approach, that low ice concentrations can be generated by homogeneous nucleation if the cooling driving the supersaturation is replaced by warming within the duration of the nucleation event. Such cooling/warming can be attributed to fast changes of phase in high-frequency gravity waves (Dinh et al., 2016; Jensen et al., 2010; Spichtinger & Krämer, 2013). However, Jensen et al. (2016a) argued that the overall impact of the high-frequency waves is to increase ice concentrations produced by homogeneous freezing; the quenching of ice nucleation would only represent 11% of the events. In some infrequent cases, TTL cirrus have been observed with ice concentrations above several thousand per liter (Jensen et al., 2013; Krämer et al., 2020), in which case homogeneous nucleation is the only plausible explanation.

High altitude cirrus are common over tropical oceans, and occur with highest frequency over the central and western Pacific, followed by the Indian Ocean (Massie et al., 2010; Sassen et al., 2008). Instrumented aircraft missions from programs like CRAVE (Costa Rica Aura Validation Experiment, e.g., Jensen et al., 2008; Lawson et al., 2008), TWP-ICE (Tropical Warm Pool International Cloud Experiment, e.g., McFarquhar et al., 2007), ATTREX (Airborne Tropical Tropopause Experiment, Jensen et al., 2017), POSIDON (Pacific Oxidants, Sulfur, Ice, Dehydration, and Convection Experiment, Jensen et al., 2018) and StratoClim (Krämer et al., 2020) have provided valuable in situ observations of TTL cirrus, but have been so far mainly restricted to the Pacific Ocean or the Asian monsoon system (in the case of StratoClim). However, little effort has been dedicated to the undersampled southwestern Indian Ocean, despite the TTL cirrus occurrence reaching up to 60% during austral summer (Sassen et al., 2008).

The aim of this study is to document a singular case of in situ TTL cirrus formation around Réunion Island, in the southwestern Indian Ocean. A set of balloon-borne observations, Lagrangian trajectories and microphysical and optical calculations are presented and used to characterize the microphysical properties and the environment of the observed cirrus. The measurements presented in this study were taken in the framework of the CONCIRTO (CONvection CIRrus tropical Tropopause layer over the Indian Ocean) project. This project aims to further our understanding of deep convection and cirrus clouds and how they affect the TTL over the Indian Ocean. It funded coincidental high-resolution balloon-borne in situ measurements of water vapor, ozone, and aerosol/ice particles in austral summer 2019 (January to March). In this study, balloon-borne observations of a nascent in situ cirrus encountered on January 11, 2019 are analyzed and the results are interpreted in terms of the different cirrus formation mechanisms.

## 2. Data and Methods

### 2.1. Balloon-Borne In Situ Observations

In order to characterize the nascent TTL cirrus cloud and its environment, a Compact Optical Backscatter and Aerosol Detector (COBALD) and Cryogenic Frost Point Hygrometer (CFH) instrument were flown on the same payload on January 11, 2019. Data from the COBALD and CFH were telemetered to the ground by an Internet iMet-1-RSB meteorological radiosonde, which additionally provided measurements of ambient pressure, temperature, and wind speed and direction. The sonde was launched at 17:54 UTC from the Maito observatory ( $21.1^\circ\text{S}$ ,  $55.4^\circ\text{E}$ ), located on Réunion Island, at 2,160 m above sea level.

The COBALD backscatter instrument, developed at ETHZ (Swiss Federal Institute of Technology Zurich), uses two light-emitting diodes at two wavelengths centered at 455 and 940 nm (blue and infrared, respectively) to detect and characterize cloud and aerosol particles in the atmosphere (e.g., Brabec et al., 2012;

Brunamonti et al., 2018). The detector has a field of view of  $\pm 6^\circ$ , and the signal detected typically originates from a distance of 0.5–10 m from the sonde. Beyond 10 m, the signal becomes negligible.

For each of the two COBALD wavelengths, the COBALD raw signal is converted to backscatter ratio (BSR), which is defined as:

$$BSR = \frac{\beta_{tot}}{\beta_{mol}} = \frac{\beta_{mol} + \beta_{part}}{\beta_{mol}} = 1 + PBSR \quad (1)$$

where PBSR is the particle BSR;  $\beta_{tot}$  is the measured backscatter coefficient, expressed as the sum of the molecular ( $\beta_{mol}$ ) and particle ( $\beta_{part}$ ) contributions. The particle backscatter coefficient includes aerosols, which are mainly sulfates in the TTL or lower stratosphere, and ice crystals ( $\beta_{ice}$ ). The molecular backscatter coefficient is computed according to Bucholtz (1995), for stratospheric conditions, corresponding to 100 hPa and 203 K. The precision of the BSR resulting from the COBALD postprocessing is around 1% in the TTL with an absolute accuracy of better than 5% (Vernier et al., 2015).

The color index (CI) is defined as the ratio of the particle BSRs at the infrared and blue wavelengths:

$$CI = \frac{PBSR_{940}}{PBSR_{455}} \quad (2)$$

which is independent of number concentration but depends on the size of the particles.

The CFH, developed by Vömel et al. (2007), provides accurate water vapor measurements from the surface to the middle stratosphere. The instrument measures the frost point temperature, which combined with temperature measurements from the iMet-1-RSB allows water vapor mixing ratio and supersaturation ( $S_i$ ) to be calculated using a saturation vapor pressure formula such as Murphy and Koop (2005)—see their Equation 7. CFH water vapor mixing ratio uncertainties are 5% in the tropical troposphere (Vömel et al., 2007) and 2%–3% in the stratosphere (Vömel et al., 2016). At the one per second telemetry data rate, the CFH and COBALD have a high vertical resolution of 2–3 m with a mean balloon ascent rate of 2–3 m s<sup>-1</sup> on January 11, 2019. We use the pressure measured by Internet iMet-1-RSB as the main vertical coordinate for all instruments. All variables are binned in pressure intervals of 1 hPa (corresponding to a vertical resolution of ~25 m in the TTL) to reduce measurement noise (Brunamonti et al., 2018).

## 2.2. FLEXPART Lagrangian Model

The origin of air masses sampled at the Maïdo Observatory is assessed using the FLEXPART Lagrangian Particle Dispersion Model (Stohl et al., 2005). This transport model is run backward in time and is driven using European Centre for Medium Range Weather Forecasts—Integrated Forecast System (ECMWF-IFS) analysis (at 00, 12 UTC) and hourly forecast fields. To compute the FLEXPART trajectories, the ECMWF meteorological fields are retrieved at 0.50° and 0.15° and on full model levels (137 vertical model levels with a top at 0.01 hPa). Further details on the model set-up are described in Evan et al. (2020). Here, 100,000 air parcels were distributed randomly within boxes with a depth of 500 m and 0.10° × 0.10° longitude-latitude bins centered on the balloon at the cold-point tropopause when the cirrus was observed.

## 2.3. Microphysical and Optical Modeling

To estimate the microphysical properties of the cirrus from the COBALD BSRs, we model the backscatter signal in a similar way as in the Zürich Optical and Microphysical Model (Brabec et al., 2012; Cirisan et al., 2014). A lognormal distribution of spherical ice crystals population is assumed, following Deshler et al. (2003):

$$n(\ln r) = \frac{N_0}{\sqrt{2\pi \ln \sigma}} \exp \left( \frac{-\ln^2 \left( \frac{r}{r_M} \right)}{2 \ln^2 \sigma} \right) \quad (3)$$

where  $r_M$  is the mode radius,  $\sigma$  is the geometric standard deviation parameterizing the distribution width, and  $N_0$  is the total number concentration. This size distribution possesses three degrees of freedom,  $r_M$ ,  $\sigma$ , and  $N_0$ , thus it cannot be fully constrained by the two COBALD measurements (BSR<sub>455</sub> and BSR<sub>940</sub>). Assuming the crystals sphericity is a fair approximation under TTL conditions (Woods et al., 2018).

The backscatter coefficient from this distribution is evaluated as:

$$\beta_{ice} = \int Q_{sc}(x) \pi r^2 n(\ln r) d \ln r \quad (4)$$

where  $Q_{sc}(x)$  is the efficiency of the backward scattering to the  $\pm 6^\circ$  COBALD field of view for a single ice crystal, depending on the size parameter  $x = 2\pi r/\lambda$ . It is multiplied by the ice crystal geometric cross section ( $\pi r^2$  for a sphere) and summed over the size distribution.

The optical calculus is based on Mie code tabulations to simulate backscatter coefficients. For ice particles, the refractive index is set to 1.31. For each wavelength, the backscatter efficiency  $Q_{sc}$  is computed for varying  $r$  in intervals of  $d \ln r = 0.0023$ . Then, by setting  $N_0 = 1 \text{ cm}^{-3}$ , Equation 4 provides the backscatter coefficient for a size distribution of one particle per cubic centimeter with a mode radius  $r_M$  and width  $\sigma$ . The PBSR is computed by dividing  $\beta_{ice}$  by the molecular backscatter coefficient, taken again from Bucholtz (1995). For mode radii below  $1 \mu\text{m}$  (in the blue) and below  $2 \mu\text{m}$  (in the infrared), the backscatter coefficient weighted by the distribution (i.e., calculated as in Equation 4 but without the cross section term) is found to linearly track  $r_M$ . Up to these mode radius limits, the PBSR scales with the particle volume, relating it directly to the ice water content (IWC). The ratio of the infrared to the blue PBSR results in the CI, see Equation 2, as function of the mode radius for each size distribution width. Without additional constraints on the particle distribution, it is difficult to identify uniquely  $r_M$  from a given CI even for a single  $\sigma$ . This limitation is inherent in the computations of the backscatter coefficients using Mie calculations. With additional constraints, however, provided by a priori knowledge of the size distributions or microphysical considerations, a mode radius can be inferred by comparing the measured CI with the simulated CI for a prescribed  $\sigma$ . This finally allows deduction of the ice number concentration and the IWC as follows.

For each wavelength and prescribed  $r_M$  and  $\sigma$ , the total particle number concentration  $N_0$  is found by scaling the ice particle concentration leading to PBSR = 1 to the observed backscatter. That scaling factor is provided by the ratio of molecular backscatter coefficient from Bucholtz (1995) to the result from Equation 4 with  $N_0 = 1 \text{ cm}^{-3}$  (as mentioned above). With this scaled  $N_0$  the IWC is computed as:

$$IWC = \frac{4\pi}{3} r_M^3 N_0 \rho_{ice} \quad (5)$$

using  $\rho_{ice} = 0.917 \times 10^6 \text{ g m}^{-3}$ .

### 3. Results and Discussion

#### 3.1. Observed Cirrus Event

The balloon was launched at 17:54 UTC and reached the cold-point temperature (CPT) of 192.6 K at  $\sim 16.5 \text{ km}$  altitude at 19:40 UTC. The vertical profiles of temperature, ascent rate, and saturation ratio with respect to ice ( $S_i$ ) retrieved by the iMet and CFH during the ascent of the balloon are shown in Figure 1. During the descent CFH did not retrieve valuable data. The blue and infrared BSRs measured by the COBALD as well as the associated CI are represented for both the ascent and descent. At the cold point, peaks in the BSRs are recorded by COBALD, suggesting the presence of ice crystals. There, the CI (light green curve) is minimum and has a value of 7.3. This CI signature is roughly 1-km deep and coincides with the BSR maxima. Just below and above the dip, the clear-sky value of the CI is roughly 10. This background value corresponds to a population of sulfate droplets on which ice crystals can grow. Concomitant with the backscatter maxima in the ascent,  $S_i$  reaches 1.5. The BSR in the blue and infrared increase at the descent, as well as the CI, that shows a peak value of 16 (dark green curve).

The ascent rate of the balloon is shown on Figure 1. It is calculated following Gallice et al. (2011) and corresponds to a 60 s-low pass filtered ascent rate profile derived from the GPS altitude data. The ascent rate is

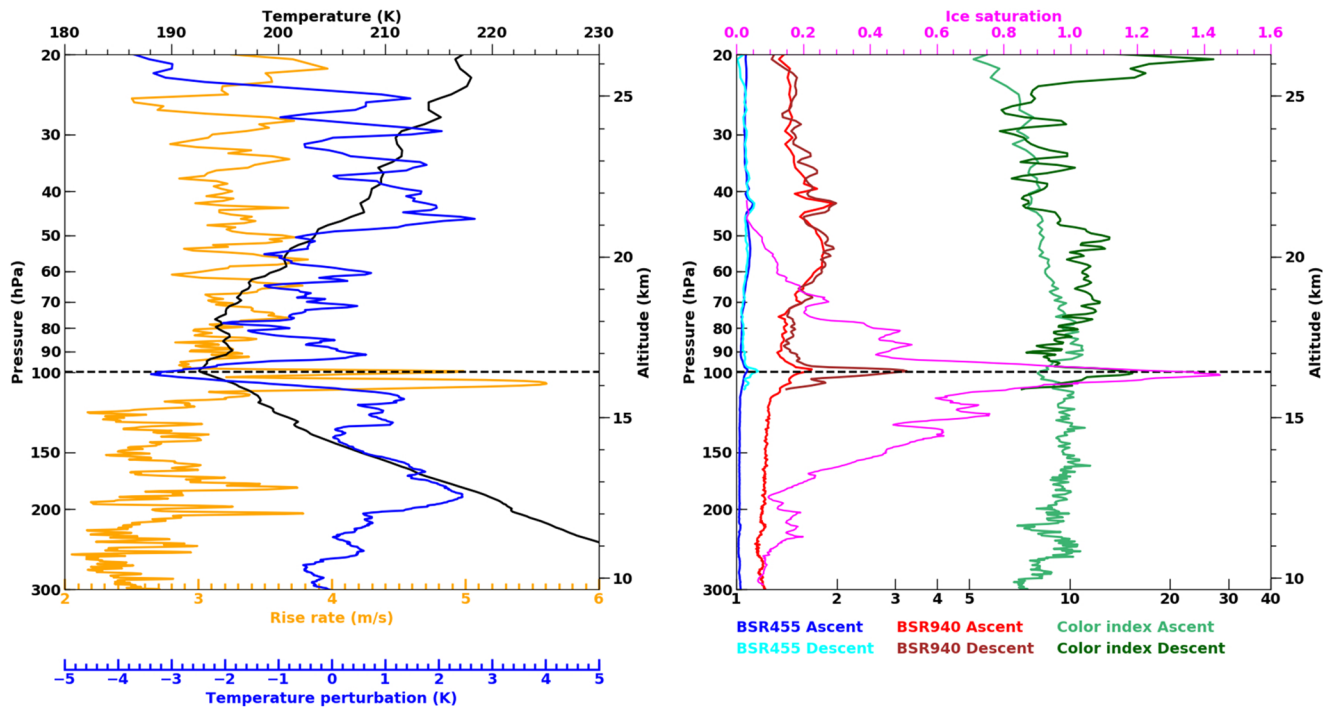


**Figure 1.** Vertical profiles measured during the sounding at Maïdo observatory on January 11, 2019 at 17:54 UTC. Left: profiles of temperature (black), temperature perturbation (blue), and ascent rate (yellow). Right: profiles of saturation ratio with respect to ice (pink), BSRs at 455 and 940 nm for the ascent (dark blue and red, respectively), and for the descent (cyan and brown, respectively) and CI at ascent/descent (light/dark green). The black dashed line corresponds to the cold point tropopause at ~16.5 km altitude.

significantly increased by 2–3  $\text{m s}^{-1}$  between 16 and 16.2 km high, just below the cold point; it is consistent with a gravity wave (GW) event that would contribute to the observed cooling/supersaturation. A mean temperature profile for January 2019 was computed using 14 radiosonde temperature profiles measured at the Maïdo Observatory from 7 to 19 January 2019. This allows the computation of the temperature anomaly (Figure 1). The characteristics of the temperature and vertical speed perturbations, most likely due to a GW event, are analyzed in Section 3.4.

### 3.2. Origin of the Sampled Air Masses

Using FLEXPART, a retrorplume consisting of 100,000 air parcels is released at 16.5 km altitude and 19:40 UTC, corresponding to the cirrus observation during the ascent. The trajectories, simulated back to 00 UTC January 11, 2019, are shown on Figure 2. Also displayed on Figure 2 are Meteosat8 brightness temperatures, from a 4-km global product merging all available geostationary satellites (Janowiak et al., 2001).

Almost all the back trajectories had their origin between 15 and 17 km. The absence of deep convective clouds along the trajectories further implies that they had not experienced deep convection, which would be consistent with in situ cirrus formation. Air masses had been advected from the south-southeast region of Réunion Island with a high moisture content, according to the ECMWF analyses (not shown). They remained within the TTL over the southwestern Indian Ocean for the full previous day (not shown).

### 3.3. Microphysical Properties of the Observed TTL Cirrus

The CI for ice and for the background sulfate aerosols is displayed in Figure 3 as function of the mode radius. To simulate the CI for ice, three different size distribution widths are used ( $\sigma = 1.3\text{--}1.6$ ) and a refractive index of 1.31. The simulated CI for sulfate aerosols is shown for a single width ( $\sigma = 1.8$ ) and refractive indexes of 1.45 and 1.51, which correspond to different  $\text{H}_2\text{SO}_4$  and  $\text{H}_2\text{O}$  proportions of the aerosols com-

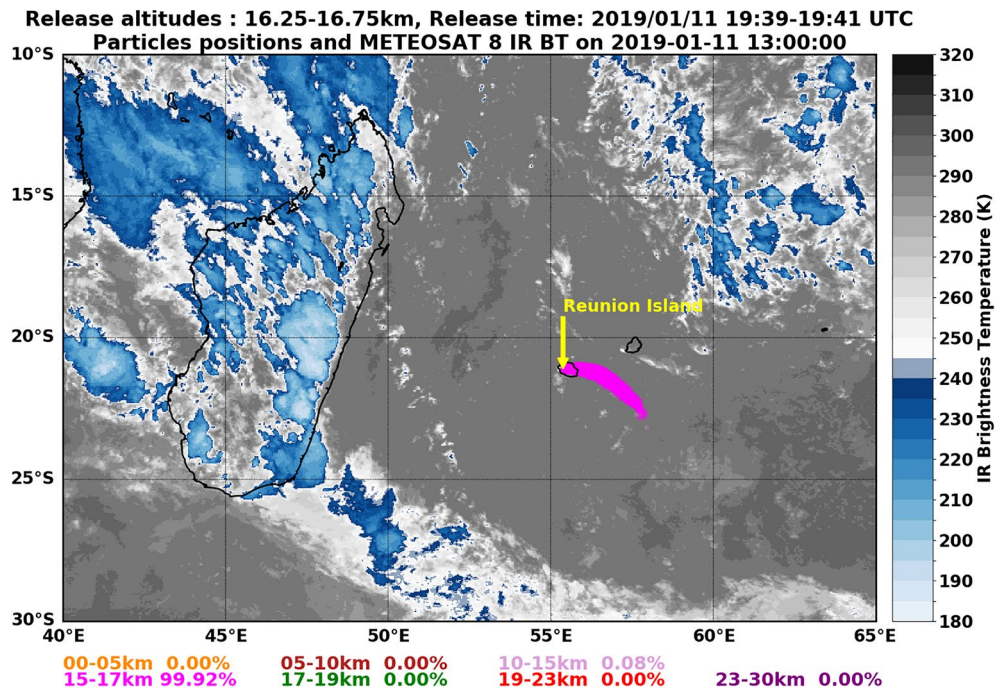


**Figure 2.** Backward trajectories from the FLEXPART model. They were initialized for the 16.25–16.75 km layer on January 11, 2019, 19:40 UTC around cirrus observation at the ascent of the balloon at the cold-point tropopause. The particle positions (pink dots) and Meteosat8 brightness temperature are shown on January 11, 2019 at 13:00 UTC, meaning that  $\sim 7$  h before the observation the particles were located in the 15–17 km altitude range.

position. These values are typical of stratospheric sulfates (Pinnick et al., 1976; Rosen & Kjome, 1991). The radius dependence of the CI is remarkably different between ice and sulfate particles. For ice, the particular dependence on  $\sigma$  and  $r_M$  between 0.5 and 2  $\mu\text{m}$  is used to constrain parameters of the size distribution.

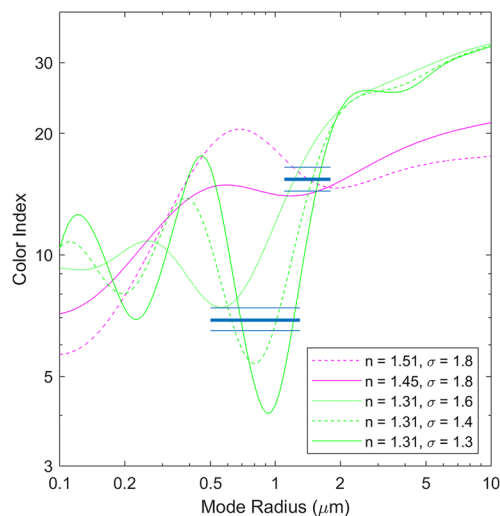


**Figure 3.** Color index versus mode radius of the ice crystals (green) and sulfate aerosols (pink). For ice, the refractive index ( $n$ ) is set to 1.31, and three different widths ( $\sigma = 1.3, 1.4,$  and  $1.6$ ) of the lognormal size distribution are used. For the sulfate aerosols, two values of the refractive index ( $n = 1.45, 1.51$ ) are used to simulate the color index for  $\sigma = 1.8$ . The blue horizontal lines indicate the CI uncertainty range for the ascent (lower lines) and descent (upper lines) observations.

At the ascent, the CI from COBALD measurements was 7.3 (Figure 1). The CI for ice, which is estimated from subtracting the background sulfates signal, is 6.9 and can be as low/high as 6.5/7.4 when accounting for the BSR uncertainty. The observed backscatter cannot be produced with particles smaller than 0.25  $\mu\text{m}$  in size. Therefore, the upper CI measurement limit implies  $\sigma$  to be less than 1.8 (the width for the sulfate aerosols) and a mode radius of at least 0.5  $\mu\text{m}$ . From the observed CI of 16 at the descent, the same analysis yields a CI for ice of 15.4 and a possible range of values from 14.4 to 16.5. These ranges of CI values are shown as blue lines in Figure 3. A single solution for the mode radius does not exist from the obtained values of CI, even when the width of the distribution is prescribed, due to the oscillations of the simulated CI. The dip that manifests for ice slightly above 0.5  $\mu\text{m}$  for a width of 1.6 sharpens and moves toward larger size as the distribution width reduces. This change of the mode that constitutes the COBALD signal typically occurs during the initial ice particles growth phase. This unique feature in CI significantly constrains the particle radii. For  $\sigma = 1.3$ –1.6 the mode radius can be constrained to 0.5–1.1  $\mu\text{m}$  during ascent and to 1.1–1.6  $\mu\text{m}$  during descent.

The ice number concentration and IWC are deduced from the obtained mode radius for a lognormal distribution with  $\sigma = 1.6$ . They are estimated to be 520  $\text{L}^{-1}$  and 0.43  $\mu\text{g m}^{-3}$  during the ascent and 42  $\text{L}^{-1}$  and 1.3  $\mu\text{g m}^{-3}$  during the descent. The uncertainties of the estimated  $N_0$  and IWC highly depend on the PBSR contribution to the BSR. In this case, the un-

certainties range between 10% and 20%. The ice number concentration is reduced by a factor of more than 10 between the ascent and the descent. Heterogeneity of microphysical properties encountered inside cirrus clouds can be explained by small-scale GWs (Jensen et al., 2013). The climatology from Krämer et al. (2020) shows (in their Figure 8) that ice concentrations (for radius above 3  $\mu\text{m}$ ) in young cirrus are most frequently around 100  $\text{L}^{-1}$ . Although cirrus with ice concentrations above 10,000  $\text{L}^{-1}$  have already been observed (Jensen et al., 2009; Krämer et al., 2009, 2020), only less than 10% of the observed TTL ice concentrations exceed 1,000  $\text{L}^{-1}$  (Krämer et al., 2020). The estimated IWC values have been previously reported in the same temperature range from in situ retrievals, but lie in the lower edge of the observed range (Krämer et al., 2016, 2020). During ATTREX 2014 over the western Pacific, direct measurements of IWC were limited to 1  $\mu\text{g m}^{-3}$ . The cloud probes used could only detect ice crystals with sizes above 1  $\mu\text{m}$  (FCDP probe) or 10  $\mu\text{m}$  (2-D-S probe, Thornberry et al. [2017]). Twenty-seconds average of the FCDP data from ATTREX and POSIDON campaigns allows the sampling of larger volumes of air, leading to IWC below 0.01  $\mu\text{g m}^{-3}$ . This indicates that while our measurements are sensible, the values found are very rare. The optical depth of the cirrus layer ( $\tau_{\text{cirrus}}$ ) is further computed. The uncertainty is much higher in the blue wavelength (90%) compared to the infrared (4%–5%), as for the shorter wavelength the molecular Rayleigh scattering is 20 times stronger and the marginal particle scattering on top is much more affected by the observed error. In the infrared, the values of  $\tau_{\text{cirrus}}$  are roughly  $1\text{--}2 \times 10^{-4}$  (see supporting information Text S1 and Figure S1 for details). With these values of the optical depth, the observed cirrus is beyond satellite detection capabilities. For example, for current CALIPSO (Cloud-Aerosol Lidar and Infrared Pathfinder Satellite Observation) V4 sensitivity, the optical depth is barely below 0.003 for night detection (Melody Avery, personal communication).

Analysis of the CI indicate the ice crystals are larger during the descent. Furthermore, the high supersaturation observed by the CFH (1.5) indicates that the environment could support the nucleation and initial growth of ice crystals. A growth calculation is performed to verify the consistency of the ice crystal size change. Neglecting the time dependence of  $S_i$  and  $T$ , the growth rate of the ice crystals is estimated following Wallace and Hobbs (2006):

$$\frac{dm}{dt} = \frac{4\pi C(S_i - 1)}{f(T)} \quad (6)$$

with

$$f(T) = \left( \frac{L_s}{R_v T} - 1 \right) \frac{L_s}{\kappa T} + \frac{R_v T}{e_i(T) D} \quad (7)$$

where  $m$  is the mass of the ice crystal,  $\kappa = 2.4 \times 10^{-2} \text{ J m}^{-1} \text{ s}^{-1} \text{ K}^{-1}$  the thermal conductivity of air at 0°C (independent of pressure),  $D = 2 \times 10^{-5} \text{ m}^2 \text{ s}^{-1}$  the diffusion coefficient of water vapor in air and  $L_s = 2.85 \times 10^6 \text{ J kg}^{-1}$  the gas constant for water vapor.  $e_i(T)$  is computed using Murphy and Koop (2005) Equation 7.

For a spherical particle,  $C$  equals the radius of the crystal. Using  $dm/dt = 4\pi\rho_{\text{ice}}r^2dr/dt$  with  $\rho_{\text{ice}} = 0.917 \times 10^6 \text{ g m}^{-3}$  Equation 6 yields:

$$r(T) = \sqrt{\frac{2}{\rho_{\text{ice}}} \frac{(S_i - 1)}{f(T)} t + r_0^2} \quad (8)$$

where  $S_i = 1.5$ ,  $T = 192.6 \text{ K}$ ,  $t = 93 \text{ min}$  and  $r_0 = 0.6 \mu\text{m}$  (the estimate from COBALD in the ascent). This computation yields a radius of 6  $\mu\text{m}$ . This value is on the same order of magnitude than COBALD estimates for the descent (1.1–1.6  $\mu\text{m}$ , see Figure 3). This value is on the same order of magnitude than COBALD estimates for the descent. Moreover, given that the supersaturation was kept constant for the growth rate calculation, the radius of 6  $\mu\text{m}$  would be an upper limit. The radius obtained from the growth rate calculation is consistent with the hypothesis that the crystals size increased between the COBALD observations at ascent and descent. Given the difference in the two methods used, the agreement in the radius found is reasonable. In reality, the COBALD sampled cirrus regions separated by 88 km (73 km when accounting for the advection). Some matching technique, like the one developed by Cirisan et al. (2014), would be needed

to sample the same cirrus twice. Given the ubiquitous small-scale structure in TTL cirrus, it is challenging to relate the cloud properties at two different times and locations.

### 3.4. Possible Mechanisms of Cirrus Formation

Wavelet analysis using S-transforms (Stockwell et al., 1996) is applied to the temperature anomaly ( $T'$ ) and the ascent rate ( $w$ ) to deduce the vertical structure of the GW event that most likely triggered the perturbations. This analysis yields a vertical wavelength of 1.5 km for a wave localized near the cold-point tropopause, for both  $T'$  and  $w$  (see supporting information Text S2 and Figures S2–S4 for details on the spectral analysis). The value of 1.5 km agrees with the vertical structure of GWs previously characterized over the tropics with the use of radiosondes. Using 6-hourly radiosonde data, Tsuda et al. (1994) reported GWs with vertical wavelengths ranging from 1 to 4 km in the TTL, with a mean value of 2.5 km. Similarly, using 12-hourly radiosonde data in the equatorial western Pacific, Kim and Alexander (2015) found GWs with vertical wavelengths shorter than 2 km (value averaged over a 3-month period, cf. their Figure 5). The amplitude of the perturbations at the cold-point tropopause are estimated to be 1 K and  $0.5 \text{ m s}^{-1}$  in temperature and vertical speed, respectively. The amplitude of the temperature perturbation is consistent with Kim and Alexander (2013). They found that only 13% of the tropical temperature anomalies due to waves with less than a 3-day period at 17 km altitude had amplitudes larger than 2 K. In addition, Kim and Alexander (2015) determined that those waves with periods between 1 and 3 days accounted for a mean decrease of the CPT of  $\sim 0.6 \text{ K}$ . Theoretical or box model predictions of ice concentration at comparable temperature generally lead to higher ice concentrations (up to  $10,000 \text{ L}^{-1}$ ) compared to our results ( $\sim 500 \text{ L}^{-1}$ ) for the same vertical wind speed (e.g., Kärcher & Lohmann, 2002; Krämer et al., 2016). For our young cirrus case this difference cannot be explained by sedimentation or the entrainment of surrounding air (which might become important in longer-lived cirrus). Probably, the cirrus observed had not reached the peak ice concentration that would be produced in a persistent updraft because of the truncation of ice nucleation by the phase change of the GW (Dinh et al., 2016; Jensen et al., 2010; Spichtinger & Krämer, 2013).

These vertical wind speed and temperature anomalies at the cold-point tropopause are most likely produced by a convectively generated GW, although different convective sources could have generated the wave. For example, large-scale organized convection over Madagascar was very active a few hours before the observation (Figure 2) and also small-scale oceanic storms developed to the west of Réunion Island during the evening (not shown). To determine the source of the GW, a full ray-tracing analysis of the wave is required (e.g., Evan et al., 2012). To perform such an analysis, the complete spectral characteristics (horizontal/vertical wavelengths, intrinsic frequency) of the wave would be needed, but this is not possible with a single observation.

## 4. Summary and Conclusion

The first observational study of a nascent TTL cirrus over the southwestern Indian Ocean is presented. On January 11, 2019, a balloon was launched from Réunion Island. The retrieved data (BSR from COBALD, water vapor content and supersaturation from CFH) allow the characterization of the cirrus and environmental formation conditions. The cirrus is observed at the cold-point tropopause, at  $\sim 16.5 \text{ km}$  altitude. Back trajectories from the FLEXPART Lagrangian model and the distribution of deep convection from Meteosat8 show that the air masses sampled by the instruments at the tropopause had remained over the ocean in the TTL and had not experienced any convection during the previous day.

The CIs for ice and sulfate aerosols are simulated with an optical model for a set of lognormal (spherical) particle size distributions. The COBALD measurements for ice are compared with the simulations to constrain the parameters of the ice crystals distribution. Overall, ice crystal radii are estimated to be smaller than  $1 \mu\text{m}$  during the ascent. For a radius of  $0.6 \mu\text{m}$ , the IWC is  $0.43 \mu\text{g m}^{-3}$ . The observed supersaturation (1.5) and estimated ice concentration ( $520 \text{ L}^{-1}$ ) are consistent with homogeneous ice formation if the temperature tendency changes during the nucleation event, which can truncate the process and limit the ice concentration (e.g., Dinh et al., 2016; Spichtinger & Krämer, 2013). Spectral analysis of concomitant observed temperature and vertical wind speed anomalies observed indicates that the nucleation event was

most likely triggered by a GW event of 1 K and  $0.5 \text{ m s}^{-1}$  amplitudes, respectively. The vertical wavelength is estimated to be 1.5 km for both perturbations. Such short vertical scale GW event and subsequent cooling/cirrus formation would be difficult to represent in most current numerical weather prediction and climate models with coarse vertical resolution in the TTL/lower stratosphere.

This study presents unique and rare observations of a relatively low concentration, very optically thin cirrus ( $\tau_{\text{cirrus}} \sim 10^{-4}$ ). It might result from the quenching of the nucleation event by a high-frequency wave. Such cirrus are difficult to measure remotely or in situ by current instrumented aircraft. Thus, the occurrence frequency of these thin cirrus could be greatly underestimated in remote sensing climatologies. This emphasizes the need for a long-term monitoring system of the TTL composition, with this kind of CFH-COBALD joint measurements performed here, especially in tropical oceanic regions with scarce TTL in situ measurements (Müller et al., 2016). Adding an ozone sonde would also be valuable to better identify air mass origins. To further assess the mechanisms controlling this specific cirrus case numerical modeling is needed.

### Data Availability Statement

Data from the sounding are available at <https://lacy.univ-reunion.fr/activites/programmes-de-recherche/anr-concirto/donnees>. Meteosat8 data are accessible at [https://disc.gsfc.nasa.gov/datasets/GPM\\_MERGIR\\_1/summary](https://disc.gsfc.nasa.gov/datasets/GPM_MERGIR_1/summary). The FLEXPART code is available at <https://www.flexpart.eu/> and the ECMWF data can be accessed at <https://apps.ecmwf.int/datasets/>.

### Acknowledgments

The authors thank the two anonymous reviewers for their useful comments. The CONCIRO project was funded by the Agence Nationale de la Recherche (ANR-17-CE01-0005-01). We thank OPAR (Observatoire de Physique de l'Atmosphère à La Réunion, including Maïdo Observatory). It is part of OSU-R (Observatoire des Sciences de l'Univers à La Réunion), which is funded by Université de la Réunion, CNRS-INSU, Météo-France and the French research infrastructure ACTRIS-France (Aerosols, Clouds and Trace Gases Research Infrastructure).

### References

- Brabec, M., Wienhold, F. G., Luo, B. P., Vömel, H., Immler, F., Steiner, P., et al. (2012). Particle backscatter and relative humidity measured across cirrus clouds and comparison with microphysical cirrus modelling. *Atmospheric Chemistry and Physics*, *12*(19), 9135–9148. <https://doi.org/10.5194/acp-12-9135-2012>
- Brewer, A. (1949). Evidence for a world circulation provided by the measurements of helium and water vapour distribution in the stratosphere. *Quarterly Journal of the Royal Meteorological Society*, *75*(326), 351–363. <https://doi.org/10.1002/qj.49707532603>
- Brunamonti, S., Jorge, T., Oelsner, P., Hanumanthu, S., Singh, B. B., Kumar, K. R., et al. (2018). Balloon-borne measurements of temperature, water vapor, ozone and aerosol backscatter on the southern slopes of the Himalayas during StratoClim 2016–2017. *Atmospheric Chemistry and Physics*, *18*(21), 15937–15957. <https://doi.org/10.5194/acp-18-15937-2018>
- Bucholtz, A. (1995). Rayleigh-scattering calculations for the terrestrial atmosphere. *Applied Optics*, *34*(15), 2765–2773. <https://doi.org/10.1364/AO.34.002765>
- Cirisan, A., Luo, B., Engel, I., Wienhold, F., Sprenger, M., Krieger, U., et al. (2014). Balloon-borne match measurements of midlatitude cirrus clouds. *Atmospheric Chemistry and Physics*, *14*(14), 7341–7365. <https://doi.org/10.5194/acp-14-7341-2014>
- Cziczko, D. J., Froyd, K. D., Hoose, C., Jensen, E. J., Diao, M., Zondlo, M. A., et al. (2013). Clarifying the dominant sources and mechanisms of cirrus cloud formation. *Science*, *340*(6138), 1320–1324. <https://doi.org/10.1126/science.1234145>
- DeMott, P. J., Cziczko, D. J., Prenni, A. J., Murphy, D. M., Kreidenweis, S. M., Thomson, D. S., et al. (2003). Measurements of the concentration and composition of nuclei for cirrus formation. *Proceedings of the National Academy of Sciences of the United States of America*, *100*(25), 14655–14660. <https://doi.org/10.1073/pnas.2532677100>
- Deshler, T., Hergiv, M. E., Hofmann, D. J., Rosen, J. M., & Liley, J. B. (2003). Thirty years of in situ stratospheric aerosol size distribution measurements from Laramie, Wyoming (41°N), using balloon-borne instruments. *Journal of Geophysical Research*, *108*(D5), 4167. <https://doi.org/10.1029/2002JD002514>
- Dessler, A., Schoeberl, M., Wang, T., Davis, S., & Rosenlof, K. (2013). Stratospheric water vapor feedback. *Proceedings of the National Academy of Sciences of the United States of America*, *110*(45), 18087–18091. <https://doi.org/10.1073/pnas.1310344110>
- Dinh, T., Podglajen, A., Hertzog, A., Legras, B., & Plougonven, R. (2016). Effect of gravity wave temperature fluctuations on homogeneous ice nucleation in the tropical tropopause layer. *Atmospheric Chemistry and Physics*, *16*(1), 35–46. <https://doi.org/10.5194/acp-16-35-2016>
- Evan, S., Alexander, M. J., & Dudhia, J. (2012). Model study of intermediate-scale tropical inertia-gravity waves and comparison to TWP-ICE campaign observations. *Journal of the Atmospheric Sciences*, *69*(2), 591–610. <https://doi.org/10.1175/JAS-D-11-051.1>
- Evan, S., Brioude, J., Rosenlof, K., Davis, S. M., Vömel, H., Héron, D., et al. (2020). Effect of deep convection on the tropical tropopause layer composition over the southwest Indian Ocean during austral summer. *Atmospheric Chemistry and Physics*, *20*(17), 10565–10586. <https://doi.org/10.5194/acp-20-10565-2020>
- Forster, P. M. d. F., & Shine, K. P. (2002). Assessing the climate impact of trends in stratospheric water vapor. *Geophysical Research Letters*, *29*(6), 10-1–10-4. <https://doi.org/10.1029/2001GL013909>
- Froyd, K. D., Murphy, D. M., Sanford, T. J., Thomson, D. S., Wilson, J. C., Pfister, L., & Lait, L. (2009). Aerosol composition of the tropical upper troposphere. *Atmospheric Chemistry and Physics*, *9*(13), 4363–4385. <https://doi.org/10.5194/acp-9-4363-2009>
- Fueglistaler, S., Dessler, A., Dunkerton, T., Folkins, I., Fu, Q., & Mote, P. W. (2009). Tropical tropopause layer. *Reviews of Geophysics*, *47*(1), RG1004. <https://doi.org/10.1029/2008RG000267>
- Gallice, A., Wienhold, F. G., Hoyle, C. R., Immler, F., & Peter, T. (2011). Modeling the ascent of sounding balloons: Derivation of the vertical air motion. *Atmospheric Measurement Techniques*, *4*(10), 2235–2253. <https://doi.org/10.5194/amt-4-2235-2011>
- Janowiak, J. E., Joyce, R. J., & Yarosh, Y. (2001). A real-time global half-hourly pixel-resolution infrared dataset and its applications. *Bulletin of the American Meteorological Society*, *82*(2), 205–218. [https://doi.org/10.1175/1520-0477\(2001\)082<0205:ARTGHH>2.3.CO;2](https://doi.org/10.1175/1520-0477(2001)082<0205:ARTGHH>2.3.CO;2)
- Jensen, E. J., Diskin, G., Lawson, R. P., Lance, S., Bui, T. P., Hlavka, D., et al. (2013). Ice nucleation and dehydration in the tropical tropopause layer. *Proceedings of the National Academy of Sciences of the United States of America*, *110*(6), 2041–2046. <https://doi.org/10.1073/pnas.1217104110>

- Jensen, E. J., Kärcher, B., Ueyama, R., Pfister, L., Bui, T. V., Diskin, G. S., et al. (2018). Heterogeneous ice nucleation in the tropical tropopause layer. *Journal of Geophysical Research: Atmospheres*, 123(21), 12210–12227. <https://doi.org/10.1029/2018JD028949>
- Jensen, E. J., Lawson, P., Baker, B., Pilon, B., Mo, Q., Heymsfield, A. J., et al. (2009). On the importance of small ice crystals in tropical anvil cirrus. *Atmospheric Chemistry and Physics*, 9(15), 5519–5537. <https://doi.org/10.5194/acp-9-5519-2009>
- Jensen, E. J., & Pfister, L. (2004). Transport and freeze-drying in the tropical tropopause layer. *Journal of Geophysical Research*, 109, D02207. <https://doi.org/10.1029/2003JD004022>
- Jensen, E. J., Pfister, L., Bui, T. V., Lawson, P., Baker, B., Mo, Q., et al. (2008). Formation of large ( $\approx 100 \mu\text{m}$ ) ice crystals near the tropical tropopause. *Atmospheric Chemistry and Physics*, 8(6), 1621–1633. <https://doi.org/10.5194/acp-8-1621-2008>
- Jensen, E. J., Pfister, L., Bui, T., Lawson, P., & Baumgardner, D. (2010). Ice nucleation and cloud microphysical properties in tropical tropopause layer cirrus. *Atmospheric Chemistry and Physics*, 10(3), 1369–1384. <https://doi.org/10.5194/acp-10-1369-2010>
- Jensen, E. J., Pfister, L., Jordan, D. E., Bui, T. V., Ueyama, R., Singh, H. B., et al. (2017). The NASA airborne tropical tropopause experiment: High-altitude aircraft measurements in the tropical western Pacific. *Bulletin of the American Meteorological Society*, 98(1), 129–143. <https://doi.org/10.1175/BAMS-D-14-00263.1>
- Jensen, E. J., Toon, O. B., Pfister, L., & Selkirk, H. B. (1996). Dehydration of the upper troposphere and lower stratosphere by subvisible cirrus clouds near the tropical tropopause. *Geophysical Research Letters*, 23(8), 825–828. <https://doi.org/10.1029/96GL00722>
- Jensen, E. J., Ueyama, R., Pfister, L., Bui, T. V., Alexander, M. J., Podglajen, A., et al. (2016a). High-frequency gravity waves and homogeneous ice nucleation in tropical tropopause layer cirrus. *Geophysical Research Letters*, 43(12), 6629–6635. <https://doi.org/10.1002/2016GL069426>
- Jensen, E. J., Ueyama, R., Pfister, L., Bui, T. V., Lawson, R. P., Woods, S., et al. (2016b). On the susceptibility of cold tropical cirrus to ice nuclei abundance. *Journal of the Atmospheric Sciences*, 73(6), 2445–2464. <https://doi.org/10.1175/JAS-D-15-0274.1>
- Kärcher, B., & Lohmann, U. (2002). A parameterization of cirrus cloud formation: Homogeneous freezing of supercooled aerosols. *Journal of Geophysical Research*, 107(D2), AAC-4. <https://doi.org/10.1029/2001JD000470>
- Kim, J.-E., & Alexander, M. J. (2013). A new wave scheme for trajectory simulations of stratospheric water vapor. *Geophysical Research Letters*, 40(19), 5286–5290. <https://doi.org/10.1002/grl.50963>
- Kim, J.-E., & Alexander, M. J. (2015). Direct impacts of waves on tropical cold point tropopause temperature. *Geophysical Research Letters*, 42(5), 1584–1592. <https://doi.org/10.1002/2014GL062737>
- Koop, T., Luo, B., Tsias, A., & Peter, T. (2000). Water activity as the determinant for homogeneous ice nucleation in aqueous solutions. *Nature*, 406(6796), 611–614. <https://doi.org/10.1038/35020537>
- Krämer, M., Rolf, C., Luebke, A., Afchine, A., Spelten, N., Costa, A., et al. (2016). A microphysics guide to cirrus clouds – Part 1: Cirrus types. *Atmospheric Chemistry and Physics*, 16, 3463–3483. <https://doi.org/10.5194/acp-16-3463-2016>
- Krämer, M., Rolf, C., Spelten, N., Afchine, A., Fahey, D., Jensen, E., et al. (2020). A microphysics guide to cirrus – Part 2: Climatologies of clouds and humidity from observations. *Atmospheric Chemistry and Physics*, 20(21), 12569–12608. <https://doi.org/10.5194/acp-20-12569-2020>
- Krämer, M., Schiller, C., Afchine, A., Bauer, R., Gensch, I., Mangold, A., et al. (2009). Ice supersaturations and cirrus cloud crystal numbers. *Atmospheric Chemistry and Physics*, 9(11), 3505–3522. <https://doi.org/10.5194/acp-9-3505-2009>
- Lawson, R. P., Pilon, B., Baker, B., Mo, Q., Jensen, E., Pfister, L., & Bui, P. (2008). Aircraft measurements of microphysical properties of subvisible cirrus in the tropical tropopause layer. *Atmospheric Chemistry and Physics*, 8(6), 1609–1620. <https://doi.org/10.5194/acp-8-1609-2008>
- Massie, S. T., Gille, J., Craig, C., Khosravi, R., Barnett, J., Read, W., & Winker, D. (2010). HIRDLS and CALIPSO observations of tropical cirrus. *Journal of Geophysical Research*, 115, D00H11. <https://doi.org/10.1029/2009JD012100>
- McFarquhar, G. M., Um, J., Freer, M., Baumgardner, D., Kok, G. L., & Mace, G. (2007). Importance of small ice crystals to cirrus properties: Observations from the tropical warm pool international cloud experiment (TWP-ICE). *Geophysical Research Letters*, 34, L13803. <https://doi.org/10.1029/2007GL029865>
- Müller, R., Kunz, A., Hurst, D. F., Rolf, C., Krämer, M., & Riese, M. (2016). The need for accurate long-term measurements of water vapor in the upper troposphere and lower stratosphere with global coverage. *Earth's Future*, 4(2), 25–32. <https://doi.org/10.1002/2015EF000321>
- Murphy, D. M., & Koop, T. (2005). Review of the vapour pressures of ice and supercooled water for atmospheric applications. *Quarterly Journal of the Royal Meteorological Society*, 131(608), 1539–1565. <https://doi.org/10.1256/qj.04.94>
- Pinnick, R., Rosen, J., & Hofmann, D. (1976). Stratospheric aerosol measurements III: Optical model calculations. *Journal of the Atmospheric Sciences*, 33(2), 304–314. [https://doi.org/10.1175/1520-0469\(1976\)033<0304:SAMIOM>2.0.CO;2](https://doi.org/10.1175/1520-0469(1976)033<0304:SAMIOM>2.0.CO;2)
- Rosen, J. M., & Kjöme, N. T. (1991). Backscattersonde: A new instrument for atmospheric aerosol research. *Applied Optics*, 30(12), 1552–1561. <https://doi.org/10.1364/AO.30.001552>
- Sassen, K., Wang, Z., & Liu, D. (2008). Global distribution of cirrus clouds from Cloudsat/Cloud-Aerosol Lidar and Infrared Pathfinder Satellite Observations (CALIPSO) measurements. *Journal of Geophysical Research*, 113, D00A12. <https://doi.org/10.1029/2008JD009972>
- Solomon, S., Rosenlof, K. H., Portmann, R. W., Daniel, J. S., Davis, S. M., Sanford, T. J., & Plattner, G.-K. (2010). Contributions of stratospheric water vapor to decadal changes in the rate of global warming. *Science*, 327(5970), 1219–1223. <https://doi.org/10.1126/science.1182488>
- Spichtinger, P., & Krämer, M. (2013). Tropical tropopause ice clouds: A dynamic approach to the mystery of low crystal numbers. *Atmospheric Chemistry and Physics*, 13(19), 9801–9818. <https://doi.org/10.5194/acp-13-9801-2013>
- Stockwell, R. G., Mansinha, L., & Lowe, R. (1996). Localization of the complex spectrum: The S transform. *IEEE Transactions on Signal Processing*, 44(4), 998–1001. <https://doi.org/10.1109/78.492555>
- Stohl, A., Forster, C., Frank, A., Seibert, P., & Wotawa, G. (2005). Technical note: The Lagrangian particle dispersion model FLEXPART version 6.2. *Atmospheric Chemistry and Physics*, 5(9), 2461–2474. <https://doi.org/10.5194/acp-5-2461-2005>
- Thornberry, T. D., Rollins, A. W., Avery, M. A., Woods, S., Lawson, R. P., Bui, T. V., & Gao, R.-S. (2017). Ice water content-extinction relationships and effective diameter for TTL cirrus derived from in situ measurements during ATTREX 2014. *Journal of Geophysical Research: Atmospheres*, 122(8), 4494–4507. <https://doi.org/10.1002/2016JD025948>
- Tsuda, T., Murayama, Y., Wiryosumarto, H., Harijono, S. W. B., & Kato, S. (1994). Radiosonde observations of equatorial atmosphere dynamics over Indonesia: 2. Characteristics of gravity waves. *Journal of Geophysical Research*, 99(D5), 10507–10516. <https://doi.org/10.1029/94JD00354>
- Vernier, J.-P., Fairlie, T., Natarajan, M., Wienhold, F., Bian, J., Martinsson, B., et al. (2015). Increase in upper tropospheric and lower stratospheric aerosol levels and its potential connection with Asian pollution. *Journal of Geophysical Research: Atmospheres*, 120(4), 1608–1619. <https://doi.org/10.1002/2014JD022372>

- Vömel, H., David, D. E., & Smith, K. (2007). Accuracy of tropospheric and stratospheric water vapor measurements by the cryogenic frost point hygrometer: Instrumental details and observations. *Journal of Geophysical Research*, *112*, D08305. <https://doi.org/10.1029/2006JD007224>
- Vömel, H., Naebert, T., Dirksen, R., & Sommer, M. (2016). An update on the uncertainties of water vapor measurements using cryogenic frost point hygrometers. *Atmospheric Measurement Techniques*, *9*(8), 3755–3768. <https://doi.org/10.5194/amt-9-3755-2016>
- Wallace, J. M., & Hobbs, P. V. (2006). *Atmospheric science: An introductory survey (Vol. 92)*. Elsevier.
- Woods, S., Lawson, R. P., Jensen, E., Bui, T., Thornberry, T., Rollins, A., et al. (2018). Microphysical properties of tropical tropopause layer cirrus. *Journal of Geophysical Research: Atmospheres*, *123*(11), 6053–6069. <https://doi.org/10.1029/2017JD028068>